TEXTURAL ANALYSIS FOR CRACK-DETECTION USING INFRARED THERMOGRAPHY, VISUAL COLOUR, AND GREYSCALE CONCRETE IMAGERY

Shahid Kabir [1], Patrice Rivard [2], Gérard Ballivy [3] and Dong-Chen He [4]

ABSTRACT

Imaging-based inspection methods are increasingly being employed for damage assessment in concrete structures due to the development of advanced non-destructive testing (NDT) techniques. These methods can provide quantitative information while reducing the time and cost involved, compared to inspections based solely on conventional visual approaches. However, in order to extract accurate data from the images, efficient image analysis methods need to be developed. This study proposes the application of the grey level co-occurrence matrix (GLCM) texture analysis approach, through which surface deterioration features in the concrete imagery are extracted. An artificial neural network (ANN) classifier is also employed to obtain damage information, such as the total amount of superficial cracking, as well as the total length, and range of crack widths. These methods were applied to thermographic, visual color and greyscale images of concrete blocks that were exposed outdoors for ten years, as well as slabs that were kept indoors, all specimens exhibiting various levels of alkali-aggregate reaction (AAR) damage. The results show that all three types of imagery are relatively effective in characterizing and quantifying crack damage; however, the infrared thermography produced more accurate results compared to the visual color, and grey scale images.

KEYWORDS

alkali-aggregate reaction (AAR), artificial neural networks (ANN), concrete imaging, damage assessment, GLCM texture analysis, infrared thermography.

INTRODUCTION

The deteriorating condition of concrete structures and the excessive costs required for their replacement, rehabilitation or repair necessitate the development of innovative and effective inspection and evaluation tools. Such tools will assist in estimating the current condition and future performance of concrete structures, and in determining the appropriate allocation of funds in order to optimize maintenance, improve serviceability and minimize life-cycle costs. Periodic inspection and maintenance of concrete structures is thus necessary to keep them operational and to avoid major replacement or repairs (Abudayyeh et al. 2004).

[1] Researcher, Groupe de Recherche sur l'Auscultation et l'Instrumentation (GRAI), Univ. of Sherbrooke, Québec, J1K 2R1, Tel 819/821-8000, FAX 819/821-7974, Shahid.Kabir@Usherbrooke.ca

[2] Professor, Civil Engrg. Department, Univ. of Sherbrooke, Québec, Canada J1K 2R1, Tel 819/821-8000, FAX 819/821-7974, Patrice.Rivard@Usherbrooke.ca

[3] Professor, Civil Engrg. Department, Univ. of Sherbrooke, Québec, Canada J1K 2R1, Tel 819/821-8000, FAX 819/821-7974, Gerard.Ballivy@Usherbrooke.ca

[4] Professor, Centre d'applications et de recherches en télédétection (CARTEL), Univ. of Sherbrooke, Québec, Canada J1K 2R1, Tel 819/821-8000, FAX 819/821-7944, Dong-Chen.He@Usherbrooke.ca

Conventional evaluation methods for concrete structures, such as highway bridges, are mainly based on visual inspections, where trained inspectors examine the various components of a structure using non-destructive testing (NDT) techniques, evaluate the condition of the components, and give them a ranking (Washer 1998). Although visual inspection may be effective in many cases, it is costly, time-consuming, and often a disruption to traffic. Also, this evaluation is subjective in nature and strongly depends on the experience and skill of the inspectors; the lack of objective and quantitative information can produce significant differences between the estimated and the actual condition of a structure, and the amount of repair work needed.

Imaging in NDT is generally used to improve inspection reliability, to improve damage detection and characterization, to automate inspection tasks and to generate information about the material properties to assist in assessing the remaining life of a structure (Chen 1998). Concrete imaging based on NDT methods has proven to be quite efficient in collecting large-scale data with a minimum of traffic disruption. As a result, these approaches can provide accurate, quantitative information to supplement visual inspections, thus increasing the frequency of inspections while reducing cost and time-consumption. Imaging of concrete can be achieved through a variety of approaches, such as infrared thermography, visual color and greyscale imagery. Thermal imaging is a technique for converting the measurement of infrared energy emitted by the target in a thermal radiation pattern, which is invisible to the human eye, into an accurate two-dimensional mapping, or visual image, of steady or transient thermal effects through the use of an infrared camera (Clark et al. 2003). Visual colour and greyscale imagery of concrete greatly extend natural vision capabilities in terms of colour and greyscale perception. Human vision is relatively poor at differentiating the brightness and colour features in the scene being viewed, whereas greyscale digital imagery can provide hundreds of levels of grey and colour digital imaging allows the quantitative differentiation of millions of different colours. Such a range of image perception is unattainable by the human eye, but is extremely useful for quantitative image analysis.

There is, however, a need for the development of effective image analysis techniques in order to derive the information needed from the concrete imagery. This study proposes that texture information extracted through the grey level co-occurrence matrix texture analysis approach can improve the detection of deterioration features in the concrete imagery and that the artificial neural network classifier can be employed for more accurate damage characterization and assessment. These methods are evaluated through the use of three different image sources, infrared thermography, visual colour and greyscale, in order to determine their effectiveness.

THEORETICAL BACKGROUND

STATISTICAL TEXTURE ANALYSIS

Statistical texture methods analyze the spatial distribution of grey values in an image by computing local features at each point in the image, and deriving a set of statistics from the distributions of the local features. Depending on the number of pixels defining the local feature, statistical methods can be classified into first-order (one pixel), second-order (two pixels) and higher-order (three or more pixels) statistics. The basic difference is that first-

order statistics estimate properties of individual pixel values, ignoring the spatial interaction between image pixels, whereas second- and higher-order statistics estimate properties of two or more pixel values occurring at specific locations relative to each other (Jensen 2000).

Texture analysis rarely uses individual properties of the statistics. Instead, statistical features are derived for the extraction of textural information from the image. These features are obtained through processes that take measured grey values to compute new values. For second-order statistics, the grey values in a window of specific size are taken and the result of the computations is written back on the central pixel; this process is repeated for all pixels in the image. The outputs of the derived features are images in which the pixel values have been changed to reflect a particular feature, or texture; therefore, the resulting feature images are also known as texture features (Schowengerdt 1997).

Grey Level Co-occurrence Matrix

Second-order statistics operate on a probability function that measures the probability of observing a pair of grey values, separated by a certain distance and direction, occurring in the image. This probability function is also known as the co-occurrence matrix, since it measures the probability of the co-occurrence of two pixel values. As many as fourteen second-order texture features (Haralick 1979) can be derived from these statistics, such as, contrast mean, and variance, to name a few.

The success of the GLCM method depends on the choice of the distance and the direction between the pixels, and the window size. The appropriate distance between pixels depends on how fine or coarse the texture of interest is. Small distances are usually used for fine textures since pixels close to each other will present enough variation in their grey values to characterize these textures, whereas greater pixel distances are generally used for more coarse textures because variations in the grey values occur in pixels farther away from each other. It has been found that small distances produce the best results (Karathanassi et al. 2000) since they are appropriate for textures that are fine, as well as for those that are coarse. A distance of 1 pixel means that the pixels in the pair will be located right next to each other.

Concerning the direction between pixels, four directions can be used: 0º (horizontal), 45º (diagonal), 90º (vertical) and 135º (diagonal); however, selecting which direction to use can be difficult. The most common choice for the direction between pixels found in literature is 0º; this means that the two pixels will be located horizontally from each other.

The classification accuracy using texture features also depends on the size of the window used. This refers to the size of the pixel neighbourhood around a central pixel that represents a certain area in the image to be analyzed at a time; after analysis of this area, the window is shifted by one pixel to the next area in the image for analysis. A 3x3 window for example, represents an area in the image that is 3 pixels x 3 pixels. If the window is too small or too large relative to the texture structure, then real textural properties will not be accurately reflected (Jensen 2000). One method that can be used to determine the appropriate window size is by calculating the variation coefficient for each object class as a function of the size of the window, using any given texture feature (Anys 1995). The appropriate window size will be that for which the variation coefficients start to stabilize for the majority of the classes, while having the lowest value.

ARTIFICIAL NEURAL NETWORKS

Artificial neural networks (ANNs) are mathematical models designed to mimic aspects of how biological nervous systems, such as the brain, are believed to process information. An ANN is composed of a large number of parallel processing structures consisting of non-linear processing elements (neurons) interconnected by fixed or variable weights, with many inputs (either from original data or from the output of other neurons in the neural network) and one output, and can have a variety of network architectures (Haykin 1999).

The most popular network is the multi-layer perceptron (MLP), which is usually composed of three layers: an input layer, a hidden layer and an output layer. In the input layer, the number of nodes corresponds to the number of input features and the number of nodes in the output layer corresponds to the number of target classes. Typically, an input signal travels from the input layer to the hidden layer, where it passes through an activation function to compute the output from the hidden nodes. In an MLP network, the activation function most commonly used is the logistic function, since it introduces non-linearity into the network (Liu et al. 2003).

ANNs learn input-output relationships through supervised training, in which the user assembles a set of training data that contains examples of inputs together with corresponding outputs, and the network learns to infer the relationship between the two. The network is then trained using a supervised training algorithm, which uses the data to adjust the network so as to minimize the error in its outputs compared to the actual outputs of the training set; the most common algorithm used for the MLP is the error back-propagation method (Awcock 1996). The training procedure ends when the error is reduced to a pre-specified threshold or when it cannot be minimized any further. If the network is properly trained, it has learned to model the function that relates the input variables to the output variables, and can subsequently be used to make predictions where the output is not known.

METHODS AND RESULTS

MATERIALS

Images were taken of concrete specimens exhibiting various levels of surface cracking associated with alkali-aggregate reaction (AAR). This reaction occurs between some reactive aggregates and alkali hydroxides in the concrete pore solution. AAR leads to swelling and cracking of the concrete. The amount of cracking is closely related to the expansion level and other indicators of concrete deterioration, such as loss of rigidity, decreasing mechanical properties, etc. (Rivard and Ballivy 2005).

Measurements were conducted on two sets of concrete specimens. The first set consists of three concrete blocks (40 cm × 40 cm × 70 cm in size), which were exposed outdoors to the elements for over ten years at the CANMET site in Ottawa (Canada). The second set consists of three concrete slabs (100 cm × 100 cm × 25 cm in size) batched and kept at the GRAI laboratory (University of Sherbrooke). These slabs were wrapped with damp terry cloth and stored at ambient air (20 ± 2°C). In order to estimate the amount of inner damage, compression (*P*) wave velocities were measured through the Impact-echo method on the CANMET and GRAI specimens. It is known that velocities decrease with increasing amount

of damage (Carino 2003). Expansion was measured using stainless steel studs that were fixed on the top surface and on the sides of the specimens. Table 1 provides details on the concrete mixtures, average expansion levels and *P*-wave velocities.

Table 1: Mixture Proportions, Average *P*-wave Velocities and Expansion Measurements of CANMET and GRAI Specimens

	CANMET			GRAI		
	D1	**D2**	**D3**	**D1**	**D2**	**D3**
W / C	0.42	0.42	0.42	0.75	0.66	0.66
Cement content (kg/m³)	423	423	425	210	390	390
Total Na_2O_{eq} (kg/m³)	1.69	3.81	5.31	3.81	5.25	5.25
Density (kg/m³)	2303	2303	2317	2223	2326	2340
Average expansion (%)	0.025	0.374	0.383	0.000	0.060	0.100
Average *P*-wave velocities ($m.s^{-1}$)	4909	4513	4402	n.d.	n.d	n.d

INPUT IMAGE DATA DESCRIPTION

Greyscale and colour images of the specimens were taken by digital camera and thermographic images were taken using an infrared camera, at a pixel resolution of 0.26 mm; the images were then cropped to an image matrix of 512 x 512 pixels. All three types of imagery were processed using the GLCM texture analysis method and then classified through the ANN technique in order to characterize and quantify crack damage. These different techniques can be applied through a variety of image processing software; in this study, the Matlab software by MathWorks Inc. and the Environment for Visualizing Images (ENVI) image processing system by Research Systems Inc., were employed.

TEXTURE ANALYSIS USING GLCM

The GLCM of each image was computed based on a distance of 1 pixel and a direction of 0º between pixels, and a window size of 3x3 pixels. Although many second-order texture features can be derived from the GLCM, many of them are redundant; therefore, the software employed allows the following eight most common features by default: contrast, correlation, dissimilarity, entropy, homogeneity, mean, second moment and variance.

Since many of these texture features are redundant and capture similar concepts, features that do not help discrimination should be discarded (Richards and Jia 1999). The most effective texture features are selected through a process consisting of visual analysis, histogram analysis, and analysis of correlation matrices. In this study, the thermographic image of the CANMET-D3 specimens presented the most textural variation. As a result, this image was used in the feature selection process, since texture features found appropriate for this image, which contains the most heterogeneity, will be suitable for images that are more homogeneous as well. For feature selection of the second-order statistics, visual analysis of the feature images revealed that the contrast and entropy texture features presented poor quality in terms of visual information. Display of the histograms indicated that the two features, contrast and entropy, should be considered for elimination, and indicated the possible elimination of another texture feature, correlation, as well. Finally, the correlation

matrix further confirmed the removal of the contrast, correlation and entropy texture features, as well as the second moment and variance features, due to their relatively high correlation. Thus, the mean, homogeneity and dissimilarity second-order texture features were selected.

CLASSIFICATION USING ANN

After extraction of the textural information from the images, the next step consists of classifying and quantifying the different classes of texture. For the purposes of this study, a supervised neural network classification approach was used to extract the crack patterns from the concrete imagery. The MLP architecture used in this study was composed of four input nodes to represent the following four input features: the original input image and the three selected second-order features. Three output nodes were used to correspond to the following three target classes: wide crack, narrow crack and no crack. The logistic activation function, which is the most commonly used in an MLP network, was used in this study. For the training algorithm, the error back-propagation method is the most commonly used for the MLP, which was used in this study also.

In order to train the MLP, training data and testing data were selected from independent, spectrally distinct areas of the original input images. The three classes used for this study, wide crack, narrow crack, and no crack, were selected for their adequate representation of the whole image. In order to avoid poor classifications or inaccurate estimates of the elements, efforts were made to choose a sufficient number of training pixels, around ten percent of the total pixels, for each class; this was also done for the testing pixels. After regions of the image were selected as training data and testing data, the software implemented the MLP, which then performed a classification using the four input features. This was done for each type of image of each of the CANMET and GRAI specimens.

The results of the classification can be presented in two forms: a classified image, which shows the spatial distribution of the various classes where each pixel is assigned a symbol or colour that relates it to a specific class, and a table that summarizes the number of pixels in the whole image that belongs to each class. At the completion of a classification process, it is necessary to assess the accuracy of the results obtained. The Kappa coefficient, which was found to be the most appropriate index to provide classification precision (Fung and Ledrew 1988), was the method adopted in this study. Figure 1 shows the classified images obtained from all three types of imagery of the CANMET-D3 specimen.

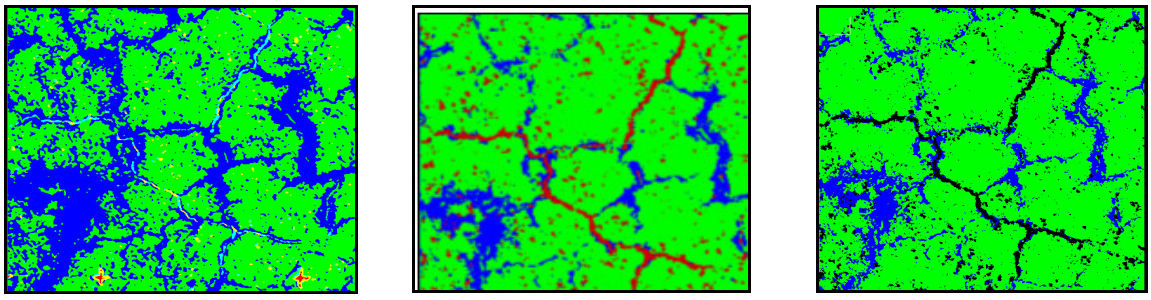

Grey level | Visual Colour | Thermography

Figure 1: Classified Images of CANMET-D3 Specimen

INTERPRETATION OF RESULTS

Results of the classifications show that the greyscale imagery performed fairly well, with an overall classification accuracy range of 72.3% - 76.5% for the CANMET blocks, and 68.7% - 75.3% for the GRAI slabs. Classifications using the visual colour imagery were slightly better than the greyscale imagery, with accuracies ranging from 71.4% - 75.2% for CANMET blocks and 70.9% - 72.0% for the GRAI specimens. The thermographic imagery, however, produced the highest overall classification accuracies, which range from 74.5% - 76.3% for the CANMET blocks and 75.6% - 76.9% for the GRAI slabs. Table 2 shows the classification accuracies obtained for each class, as well as the Kappa coefficients and overall accuracies for each specimen.

Table 2: Classification Accuracies of CANMET and GRAI Specimens

	Thermographic			Visual Colour			Greyscale		
CANMET Blocks	D1	D2	D3	D1	D2	D3	D1	D2	D3
Kappa Coefficient	0.73	0.73	0.74	0.69	0.71	0.74	0.74	0.73	0.76
Overall Accuracy (%)	74.5	73.1	76.3	71.4	75.2	74.1	72.3	76.5	75.4
Classes	Accuracy (%)								
Wide Crack	81.3	79.9	83.5	78.6	78.1	78.4	76.8	78.1	78.4
Narrow Crack	79.7	78.6	81.5	77.7	70.9	77.5	76.3	70.9	77.5
No Crack	82.4	76.7	80.6	75.3	74.6	74.2	73.6	71.4	74.2
GRAI Slabs									
Kappa Coefficient	0.75	0.74	0.76	0.72	0.74	0.74	0.69	0.72	0.74
Overall Accuracy (%)	75.6	76.9	74.2	70.9	71.6	72.0	68.7	74.1	75.3
Classes	Accuracy (%)								
Wide Crack	76.7	78.1	80.0	73.4	76.1	79.9	70.4	77.1	79.7
Narrow Crack	74.7	75.2	73.4	70.1	72.9	73.4	73.7	72.9	73.4
No Crack	76.6	74.9	79.1	72.6	76.4	78.2	73.9	71.4	77.0

Since the infrared thermography performed better than the other two types of imagery, only the results obtained from the thermographic image classifications of the different specimens were used to determine the various levels of AAR damage. The tabular results of the thermographic classifications are presented in Table 3.

Among the CANMET blocks, the D1 specimen presented the least amount of surface deterioration, in the form of narrow cracks, for a total of 3.86%. The D2 specimen had a moderate amount of surface deterioration comprised of narrow cracks at 8.15% and wide cracks at 3.62%, for a total of 11.77% damage. The D3 specimen revealed the greatest amount of deterioration, with the highest amount of narrow cracks at 19.78%, as well as a number of wide cracks at 14.25%, for a total of 34.03% surface damage.

For the GRAI slabs, the D1 specimen had the lowest total for surface damage at 1.14%, consisting only of narrow cracks. The D2 specimen presented a slightly higher surface deterioration with a total of 5.41%, made up of a moderate amount of narrow cracks and wide cracks at 3.29% and 2.12% respectively. As with the CANMET blocks, the D3 specimen for the GRAI slabs also had the highest amount of surface deterioration, with 8.75% narrow cracks and 5.37% wide cracks, for a total of 14.12% damage.

Table 3: Tabular Representation of Thermographic Classifications

Specimens	Classes	CANMET		GRAI	
		Image Pixels	Image (%)	Image Pixels	Image (%)
D3	Wide Crack	37 356	14.25	14 078	5.37
	Narrow Crack	51 852	19.78	22 937	8.75
	No Crack	172 936	65.97	225 129	85.88
	Total Pixels	262 144	100.00	262 144	100.00
D2	Wide Crack	9 489	3.62	5 557	2.12
	Narrow Crack	21 365	8.15	8 625	3.29
	No Crack	231 290	88.23	247 962	94.59
	Total Pixels	262 144	100.00	262 144	100.00
D1	Wide Crack	0	0.00	0	0.00
	Narrow Crack	10 119	3.86	5 943	1.14
	No Crack	252 025	96.14	256 201	98.86
	Total Pixels	262 144	100.00	262 144	100.00

In order to quantify the total length of wide cracks, pixels along the length of each branch of the cracks were summed and the total multiplied by the pixel resolution of 0.26 mm. For the CANMET blocks, a total length of 237.4 mm of wide cracks was calculated for the D3 specimen, for the D2 specimen, the total length was found to be 97.6 mm, and for the D1 specimen, the total length was 0 mm. Among the GRAI slabs, the total length of wide cracks was calculated to be 0 mm, 38.6 mm and 107.3 mm for the D1, D2 and D3 specimens, respectively. Close-ups of the wide cracks in the CANMET-D3 specimen can be seen in Figure 2.

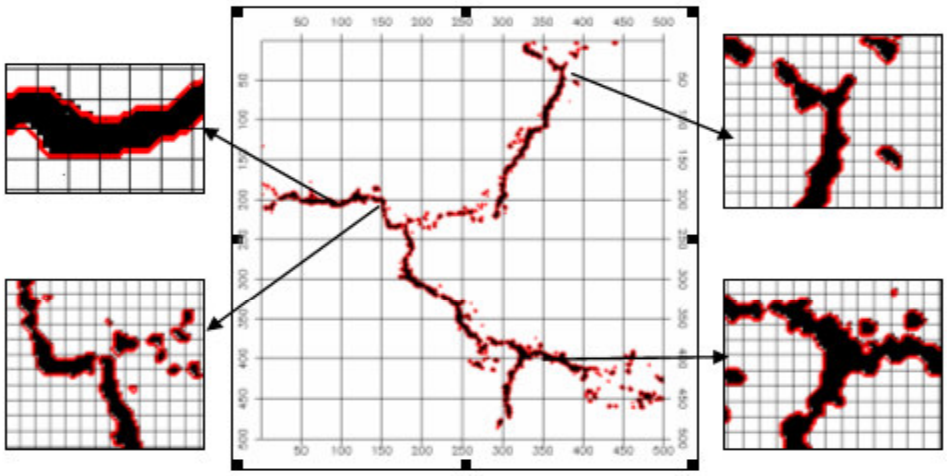

Figure 2: Wide Cracks in CANMET-D3 Specimen and Close-ups at 40x

The average crack width was determined by measuring the width of the wide cracks at several points, which correspond to the widest and the narrowest sections of the cracks. Each square represents one pixel at a resolution of 0.26 mm. As a result, the average width of cracks in the CANMET blocks was found to be 1.6 mm in the D3 specimen, 0.8 mm in the D2 specimen, and 0 mm for the D1 specimen. For the GRAI slabs, the average crack widths

were 0 mm for D1, 0.3 mm for D2 and 0.8 mm for the D3 specimen. Figure 3 provides examples of crack width measurements for the GRAI-D3 specimen.

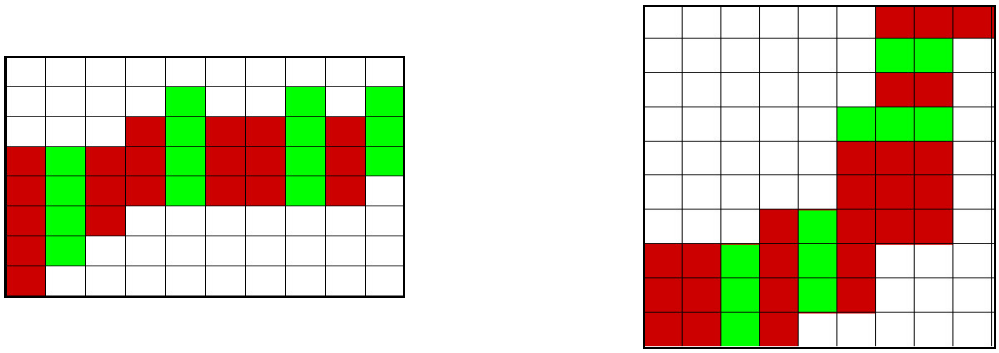

Figure 3: Crack width measurements for GRAI-D3; pixel resolution is 0.26 mm

These findings are supported by the data recorded for the CANMET and GRAI specimens (Table 1). Among the CANMET blocks, the D3 specimen was prepared with the highest alkali content, and showed the highest expansion level. On the other hand, the D1 specimen showed a lower expansion level as the concrete was mixed with a low alkali level. The highest values for the total length of wide cracks as well as for the average width of cracks found for the D3 specimen also correspond well to its having the lowest *P*-wave velocities, indicating the highest deterioration level. As for the GRAI slabs, the absence of wide cracks in the D1 specimen, which had a value of 0 mm for the average width of cracks, as well as for the total length of cracks, is corroborated by its having the lowest expansion level, indicating very little damage. A higher level of expansion was measured on the D2 specimen, with the D3 specimen having the highest measurement for expansion level among the slabs.

CONCLUSION

This approach appears to be effective in detecting and quantifying surface deterioration, such as cracks in the concrete, from thermographic, visual colour and greyscale imagery. The thermographic imagery produced the best results, since the classification accuracies obtained with this type of imagery were the highest for all the specimens. Since these methods allow for less costly and time-consuming evaluations compared with traditional visual inspection methods, evaluations can be carried out more often to supplement visual inspections. One great advantage of the IR thermography method is that the images can be acquired at night, which would cause even less traffic disruption. These techniques also allow for quantitative evaluations, such as total amount of surface damage in the images, which can improve the quality of concrete condition information obtained from traditional inspections used for making decisions concerning maintenance and repairs. For further studies these approaches can be evaluated for their potential to be used as part of a monitoring system for concrete structures, such as bridge decks and highway infrastructures. The quantitative analysis resulting from this approach can be used in the development of an automated system for damage assessment to determine the different levels of deterioration, which can be applied to a collection of concrete images for classification according to the level of surface damage.

ACKNOWLEDGEMENTS

The authors wish to thank Dr. Benoit Fournier from CANMET for the concrete specimens and GRAI for the images, laboratory and in-situ data. This project is supported by a grant from the Fonds québécois de recherche sur la nature et les technologies (FQRNT).

REFERENCES

Abudayyeh, O., Al-Bataineh, M., and Abdel-Qader, I. (2004). "An imaging data model for concrete bridge inspection." *Advances in Engineering Software,* (35) 473–480.

Anys, H. (1995). *Reconnaissance des cultures à l'aide des images radar: approche multi-polarisation et texturale*. Ph.D. Thesis, Univ. of Sherbrooke, Sherbrooke, QC, 241 pp.

Awcock, G.W., and Thomas, R. (1996). *Applied Image Processing*. McGraw-Hill, New York, 300 pp.

Carino, N. (2003). "Nondestructive Test Methods to Evaluate Concrete Structures." 6th CANMET/ACI *Int. Con. on Durability of Concrete*, June, Thessaloniki, Greece, 75 pp.

Chen, C.H. (1998). "Pattern Recognition in Non-destructive Evaluation of Materials." *Handbook of Pattern Recognition and Computer Vision*, 2nd edition, World Scientific Publishing Co., 455-471.

Clark, M.R., McCann, D.M., and Forde, M.C. (2003). "Application of Infrared Thermography to the Non-destructive Testing of Concrete and Masonry Bridges." *NDT & E International*, (36) 265-275.

Fung, T., and Ledrew, E. (1988). "The Determination of Optimal Threshold Levels for Change Detection using Various Accuracy Indices." *Photogrammetric Engineering and Remote Sensing*, 54 (10) 1449-1454.

Haralick, R.M. (1979). "Statistical and Structural Approaches to Texture." *Proceedings of the IEEE*, 67 (5) 786-804.

Haykin, S. (1999) *Neural Networks*. 2nd edition, Prentice-Hall, New Jersey.

Jensen, J.R. (2000). *Remote Sensing of the Environment: An Earth Resource Perspective*. Prentice-Hall, New Jersey, 336 pp.

Karathanassi, V., Iossifidis, C.H., and Rokos, D. (2000). "A Texture-Based Classification Method for Classifying Built Areas According to their Density." *International Journal of Remote Sensing*, 21 (9) 1807-1823.

Liu, C., Zhang, L., Davis, C.J., Solomon, D.S., Brann, T.B., and Caldwell, L.E. (2003). "Comparison of Neural Networks and Statistical Methods in Classification of Ecological Habitats using FIA Data." *Forest Science*, 49 (4) 619-631.

Richards, J.A., and Jia, X. (1999). *Remote Sensing Digital Image Analysis: An Introduction*. 3rd edition, Springer-Verlag, New York, 363 pp.

Rivard, P., and Ballivy, G. (2005). "Assessment of the Expansion Related to Alkali-Silica Reaction by the Damage Rating Index Method." *Constr. and Building Mat.*, 19 (2) 83-90.

Schowengerdt, R.A. (1997). *Remote Sensing: Models and Methods for Image Processing*. 2nd edition, Academic Press, San Diego.

Washer, G.A. (1998). "Developments for the Non-destructive Evaluation of Highway Bridges in the USA." *NDT & E International*, 31 (4) 245-249.